npj | computational materials

Article

Published in partnership with the Shanghai Institute of Ceramics of the Chinese Academy of Sciences

https://doi.org/10.1038/s41524-025-01792-2

Molecular descriptors for high-throughput virtual screening of fluorescence emitters with inverted singlet-triplet energy gaps

Check for updates

Yu Pang, Juanjuan Wang, Junfang Yang & Qian Peng ✉

The discovery of fluorescence materials with an inverted singlet-triplet (IST) energy gap, where the singlet excited state (S_1) lies below the triplet excited state (T_1), mark a transformative advancement in organic light-emitting diodes (OLEDs) technology. However, designing the potential IST emitters are greatly challenging, and their IST energy gap, arising from double electron excitation, can only be accurately described by time-consuming post-Hartree-Fock (HF) methods, which blocks large-scale high-throughput screening speed. Here, we develop a four-orbital model to elucidate detailly the roles of double excitations in the IST formation, and establish two molecular descriptors (K_S and O_D) based on exchange integral and molecular orbital energy. By these descriptors, we rapidly identify 41 IST candidates out of 3,486 molecules. The descriptors-aided approach achieves a screening success rate of 90% and reduces computational costs by 13 times compared to full post-HF calculations. Importantly, we predicted a series of excellent non-traditional near-infrared IST emitters from a dataset of 1028 compounds with emission wavelengths ranging from 852.2 to 1002.3 nm, which open new avenues for designing highly efficient near-infrared OLED materials.

Organic light-emitting diodes (OLEDs) are widely used as light sources in smartphone and TV displays, as well as in lighting panels[1]. A major challenge in the development of OLEDs is to increase the internal quantum efficiency (IQE) to achieve brighter devices[2]. In traditional fluorescent OLEDs, only 25% of singlet excitons emit light due to spin statistics, while 75% of triplet excitons are wasted[3]. To enhance IQE, thermally activated delayed fluorescence (TADF) has emerged. In TADF systems, triplet excitons are efficiently upconverted from the lowest triplet state (T_1) to the lowest excited singlet state (S_1) by a reverse intersystem crossing (rISC) process, resulting in a maximum IQE of close to 100%[4]. Nevertheless, TADF-OLEDs suffer from severe efficiency roll-off, such as triplet-triplet annihilation and triplet-polaron annihilation[5,6]. Thus, an ideal scenario would be thermodynamically favorable down-conversion with a negative singlet-triplet energy gap (ΔE_{ST}), accelerating the rISC process without requiring thermal activation, and effectively overcoming roll-off issues. Recently, azaphenalenes have gained considerable attention in the field of organic electronic materials because they exhibit an inverted singlet-triplet (IST) energy gap (a violation of Hund's rule)[7–11]. And their high stability and color tunability make them ideal candidates for applications in organic light-emitting diodes, as recently demonstrated in experimental implementations[12]. The discovery and development of IST materials mark a transformative advancement in OLED technology. By enabling efficient rISC, these materials pave the way for next-generation displays and lighting solutions with unprecedented efficiency and performance.

Recently, many theoretical studies[13–17] indicated that the participation of double electron excitation plays a necessary role in predicting Hund's rule violations, resulting in that the time-dependent density functional theory (TDDFT), a popular method for calculating the excited states, miserably failed in describing IST energy gap due to a lack of capturing double excitations. Thus, more accurate but expensive methods were adopted to predict negative ΔE_{ST}, such as spin-component-scaled coupled cluster doubles (SCS-CC2), equation-of-motion coupled cluster singles and doubles (EOM-CCSD), algebraic diagrammatic construction at the second order (ADC(2)), complete active space perturbation theory of second order (CASPT2), or n-electron valence-state perturbation theory of second order (NEVPT2)[18–22]. Although many accurate electronic structure calculations have been made, the mechanism of violations of Hund's rule is still being explored and unclear. Moreover, expensive and time-consuming calculations severely decrease the large-scale high-throughput virtual screening (HTVS) speed for discovering IST materials. Therefore, it is imperative to develop a fundamental model to disclose the mechanism of violations of Hund's rule, and construct key molecular descriptors to characterize this property, in order to realize HTVS from a large-scale chemical space.

Here, we have developed a four-orbital model (FOM) with single and double electron excitations to elucidate the roles of double excitations,

School of Chemical Sciences, University of Chinese Academy of Sciences, Beijing, PR China. ✉e-mail: qianpeng@ucas.ac.cn

energy levels, and exchange integrals of involved orbitals in the formation mechanism of IST energy gap. And the IST mechanism is revealed that the ultra-small HOMO-LUMO orbital overlaps and the significantly large energy differences between orbitals involved in double excitation synergistically induce negative ΔE_{ST}. Based on this mechanism, two molecular descriptors (K_{S} and O_{D}) are built to figure out the conditions for the occurrence of IST energy gap in azaphenalene derivatives. Using the two descriptors, 41 IST cores are rapidly screened from a chemical space of 3,486 cores. Relative to expensive post-HF calculations, the period of screening has been shortened by 13 times while the success rate of screening is as high as 90%. Importantly, a series of potential non-traditional near-infrared IST materials from a dataset of 1028 compounds are predicted with significantly intersystem crossing rate from T_1 to S_1 and radiative rates, compared to the systems that have been discovered so far. This research also marks the first time that IST materials have been predicted and proposed as near-infrared OLED emitters.

Results and discussion

Four-orbital model for IST molecules

Firstly, eight typical molecules (**1**-**8**) with IST energy gap reported in the literatures[7–9,19] and four common molecules (**9**-**12**) with normal positive singlet-triplet (PST) energy gap are selected as computational models to dissect the nature of electron transitions, as shown in Scheme 1. The geometries of 12 molecules are optimized at B3LYP/cc-pVDZ level in the S_0 state, and their excited-state properties in the S_1 and T_1 states are analyzed by ADC(2)/cc-pVDZ method which was adopted in refs. 9,11,18 (more details are found in Supplementary Information). The resultant vertical excitation energy, ΔE_{ST}, and electronic transition properties of the S_1 and T_1 states are shown in Tables S1-S4. From Table S1, it is expectedly seen that the ΔE_{ST} values of molecules **1**-**8** are negative while those of molecules **9**-**12** are positive. As stated in the references[7], the components of double excitation in both S_1 and T_1 states is very large with the values of around 10% for molecules **1**-**8**, while its component is very small in the T_1 state for molecules **9**-**12** (Table S2), which lead to their differences in ΔE_{ST}. For molecules **1**-**8**, the single electron excitations mainly happen between the highest occupied molecular orbital (HOMO) and the lowest unoccupied molecular orbital (LUMO) with proportions larger than 80%, and the double excitations involve more orbitals, primarily including HOMO-2, HOMO-1, HOMO, LUMO, LUMO + 1 and LUMO + 2 (Tables S3 and S4). Further checking the properties of orbitals, it is found that HOMO-2 and HOMO-1, LUMO + 2 and LUMO + 1 are degenerate in energy, respectively; while the energy gaps between HOMO-1 and HOMO, LUMO + 1 and LUMO are significantly large, respectively, as seen in Table S5. Thus, for simplification, it is reasonable to extract the four orbitals, HOMO-1, HOMO, LUMO, and LUMO + 1 from the multiple orbitals (Fig. 1a) to explore the mechanism of IST energy gap.

Then, a four-orbital model is constructed, including HOMO-1, HOMO, LUMO, and LUMO + 1 (Fig. 1a). The single and double electron excitation processes and their wave functions in the FOM are given in Fig. 1b. Only one single excitation between HOMO and LUMO is considered in both S_1 and T_1 states based on the discussion above, and their wave functions are denoted as $|{}^1\Psi_H^L\rangle$ and $|{}^3\Psi_H^L\rangle$, respectively. There take into account eight sets of double excitations, $|{}^1\Psi_{H,H}^{L,L}\rangle$, $|{}^1\Psi_{H,H}^{L+1,L+1}\rangle$, $|{}^1\Psi_{H-1,H-1}^{L,L}\rangle$, $|{}^1\Psi_{H-1,H-1}^{L+1,L+1}\rangle$, $|{}^1\Psi_{H,H}^{L,L+1}\rangle$, $|{}^1\Psi_{H-1,H-1}^{L,L+1}\rangle$, $|{}^1\Psi_{H,H-1}^{L,L}\rangle$ and $|{}^1\Psi_{H,H-1}^{L+1,L+1}\rangle$ for the S_1 state, and four sets of double excitations $|{}^3\Psi_{H,H}^{L,L+1}\rangle$, $|{}^3\Psi_{H-1,H-1}^{L,L+1}\rangle$, $|{}^3\Psi_{H-1,H-1}^{L,L+1}\rangle$ and $|{}^3\Psi_{H-1,H}^{L+1,L+1}\rangle$ for the T_1 state (see Fig. 1b).

Under the framework of HF theory, the wave functions ($|{}^1\Psi_H^L\rangle$ and $|{}^3\Psi_H^L\rangle$) of the S_1 and T_1 states by single excitation configuration interaction (CIS) can be expressed, and their energy difference is solved as $\Delta E_{\mathrm{ST}}^{\mathrm{CIS}} = 2K_{\mathrm{HL}}$ (the expression of the wave functions and the solution of the excited state energy are described in the "Methods" section), the K_{HL} is the exchange integral $(HL|LH)$ between the HOMO and LUMO, which is a non-negative number. Under the HF and double excitation configuration interaction (CID) approximation, the energies of S_1 and T_1 states are solved, denoted as $E_{1,\mathrm{S}}$, $E_{2,\mathrm{S}}$, $E_{3,\mathrm{S}}$, $E_{4,\mathrm{S}}$, $E_{5,\mathrm{S}}$, $E_{6,\mathrm{S}}$, $E_{7,\mathrm{S}}$ and $E_{8,\mathrm{S}}$, and $E_{1,\mathrm{T}}$, $E_{2,\mathrm{T}}$, $E_{3,\mathrm{T}}$, and $E_{4,\mathrm{T}}$ corresponding to the order of states written above, respectively. And the 32 ΔE_{ST} are obtained in CID approximation ($\Delta E_{\mathrm{ST}}^{\mathrm{CID}}$) by combining these S_1 and T_1 states. Here, the energy gap $\Delta E_{1,1}^{\mathrm{CID}}$ between $E_{1,\mathrm{S}}$ and $E_{1,\mathrm{T}}$ taken as an example in 32 $\Delta E_{\mathrm{ST}}^{\mathrm{CID}}$, their wave functions $|{}^1\Psi_{H,H}^{L,L}\rangle$ and $|{}^3\Psi_{H,H}^{L,L+1}\rangle$ are expressed see "**Methods**" section, and the corresponding $E_{1,\mathrm{S}}$ and $E_{1,\mathrm{T}}$ are obtained as:

$$E_{1,\mathrm{S}} = \left\langle {}^1\Psi_{H,H}^{L,L} | \hat{H} - E_0 | {}^1\Psi_{H,H}^{L,L} \right\rangle = 2(\varepsilon_{\mathrm{L}} - \varepsilon_{\mathrm{H}}) + J_{\mathrm{H,H}} + J_{\mathrm{L,L}} - 4J_{\mathrm{H,L}} + K_{\mathrm{H,L}} \tag{1}$$

$$\begin{aligned} E_{1,\mathrm{T}} = \left\langle {}^3\Psi_{H,H}^{L,L+1} | \hat{H} - E_0 | {}^3\Psi_{\mathrm{H,H}}^{\mathrm{L,L+1}} \right\rangle &= \varepsilon_{\mathrm{L}} + \varepsilon_{\mathrm{L+1}} - 2\varepsilon_{\mathrm{H}} + J_{\mathrm{H,H}} + J_{\mathrm{L,L+1}} - K_{\mathrm{L,L+1}} \\ &\quad -2J_{\mathrm{H,L+1}} - 2J_{\mathrm{H,L}} + K_{\mathrm{H,L+1}} + K_{\mathrm{H,L}} \end{aligned} \tag{2}$$

where ε, J and K are energy, coulomb integral $(ii|aa)$, and exchange integral $(ia|ai)$ of orbitals, respectively. Then the energy difference $\Delta E_{1,1}^{\mathrm{CID}}$ between $E_{1,\mathrm{S}}$ and $E_{1,\mathrm{T}}$ can be equal as:

$$\Delta E_{1,1}^{\mathrm{CID}} = E_{1,\mathrm{S}} - E_{1,\mathrm{T}} = \Delta\varepsilon_{1,1} + \Delta J_{1,1} + \Delta K_{1,1} \tag{3}$$

the expression of the $\Delta\varepsilon_{1,1}$, $\Delta J_{1,1}$ and $\Delta K_{1,1}$ can be seen in Supplementary Information (SI). For other cases, the derivatives of wave functions and energies of the S_1 and T_1 states, and their energy gap $\Delta E_{\mathrm{ST}}^{\mathrm{CID}}$ values are displayed in SI. The resultant $\Delta E_{\mathrm{ST}}^{\mathrm{CID}}$ can be a positive or negative number. Therefore, the total energy gap ($\Delta E_{\mathrm{ST}}^{\mathrm{tot}}$) is the sum of $\Delta E_{\mathrm{ST}}^{\mathrm{CIS}}$ and $\Delta E_{\mathrm{ST}}^{\mathrm{CID}}$, and whether its value is negative mainly depends on ε, J and K of involved orbitals, as known from Eqs. 1–3 (Fig. 1a).

The inversion mechanism of IST molecules and molecular descriptors

The molecular ε, J, K, $E_{n,\mathrm{S},1\le n\le 8}$ and $E_{n,\mathrm{T},1\le n\le 4}$ for molecules **1**-**12** are calculated at HF level (computational details seen in **SI**) and their values are summarized in Tables S6–S10. And the resultant $\Delta E_{\mathrm{ST}}^{\mathrm{CIS}}$ and $\Delta E_{\mathrm{ST}}^{\mathrm{CID}}$ are

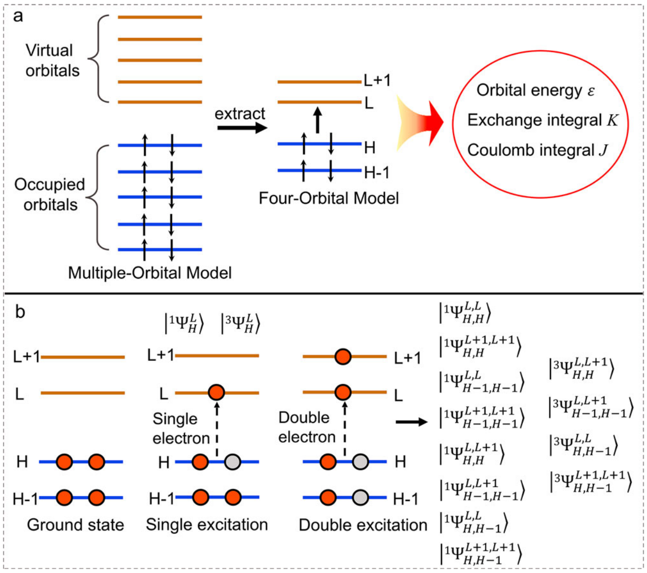
a
Virtual orbitals
Occupied orbitals
Multiple-Orbital Model
extract
L+1
L
H
H-1
Four-Orbital Model
Orbital energy ε
Exchange integral K
Coulomb integral J
b
$|{}^1\Psi_H^L\rangle$ $|{}^3\Psi_H^L\rangle$
L+1
L
H
H-1
Single electron
Double electron
Ground state
Single excitation
Double excitation
$|{}^1\Psi_{H,H}^{L,L}\rangle$
$|{}^1\Psi_{H,H}^{L+1,L+1}\rangle$
$|{}^1\Psi_{H-1,H-1}^{L,L}\rangle$
$|{}^1\Psi_{H-1,H-1}^{L+1,L+1}\rangle$
$|{}^1\Psi_{H,H}^{L,L+1}\rangle$
$|{}^1\Psi_{H-1,H-1}^{L,L+1}\rangle$
$|{}^1\Psi_{H,H-1}^{L,L}\rangle$
$|{}^1\Psi_{H,H-1}^{L+1,L+1}\rangle$
$|{}^3\Psi_{H,H}^{L,L+1}\rangle$
$|{}^3\Psi_{H-1,H-1}^{L,L+1}\rangle$
$|{}^3\Psi_{H,H-1}^{L,L}\rangle$
$|{}^3\Psi_{H,H-1}^{L+1,L+1}\rangle$

Fig. 1 | Schematic illustration of four-orbital model (FOM). a The basis of FOM. **b** The wave functions of single and double electron excitations in the S_1 and T_1 states in the FOM, H-1, H, L and L + 1 are the abbreviation of HOMO-1, HOMO, LUMO and LUMO + 1, respectively.

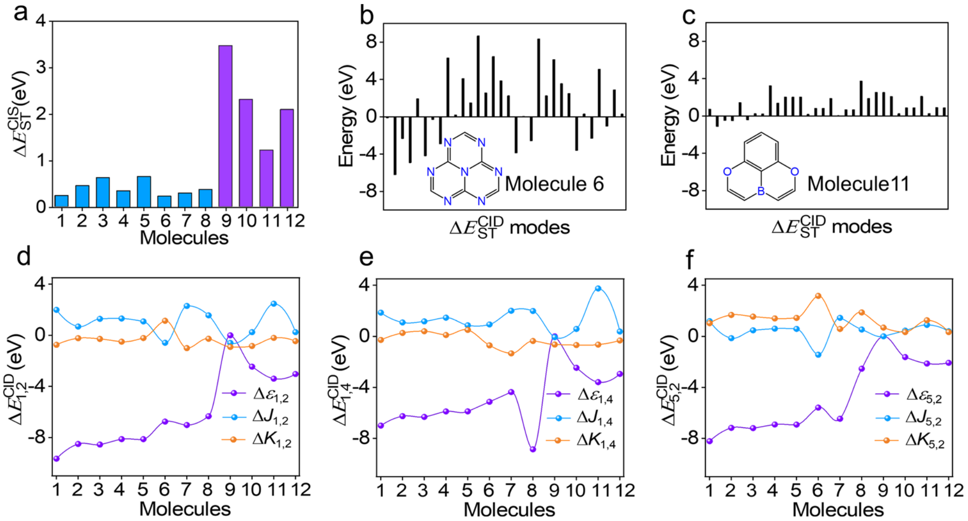

Fig. 2 | The energy decomposition analysis of singlet excitation singlet-triplet gaps and double excitation singlet-triplet gaps. **a** The singlet excitation singlet-triplet gaps ΔE_{ST}^{CIS} of molecules **1**-**12**. **b**, **c** 32 sets of double excitation singlet-triplet gaps modes for molecule **6** and **11**. **d**–**f** The energy decomposition $\Delta\varepsilon$ ($\Delta\varepsilon_{1,2}$, $\Delta\varepsilon_{1,4}$, $\Delta\varepsilon_{5,2}$), ΔJ($\Delta J_{1,2}$, $\Delta J_{1,4}$, $\Delta J_{5,2}$) and ΔK ($\Delta K_{1,2}$, $\Delta K_{1,4}$, $\Delta K_{5,2}$) of $\Delta E_{1,2}^{CID}$, $\Delta E_{1,4}^{CID}$, $\Delta E_{5,2}^{CID}$.

shown in Figs. 2a–c and S14–S25. From Fig. 2a, it is clearly seen that ΔE_{ST}^{CIS} values of molecules **1**-**8** (0.242 to 0.828 eV) are much lower than those of molecules **9**-**12** (1.220 to 3.471 eV), which is mainly caused by the K_{HL} given in Table S8 due to $\Delta E_{ST}^{CIS} = 2K_{HL}$. The K_{HL} is determined by the spatial overlap of the HOMO and LUMO. As shown in Fig. S13, the HOMO and LUMO are well-separated in space in molecules **1**-**8**, whereas exhibiting significant overlap in molecules **9**-**12**. These indicate that a small K_{HL} or slight HOMO-LUMO overlap facilitates the formation of IST energy gap. Therefore, K_{HL} is regarded as a descriptor for screening IST molecules, labeled as K_S in this work. The validity of this descriptor has been demonstrated in reference[10].

Let us move to double electron excitation properties, which is key to generate the IST. From Figs. S14-S25, it is found that in molecule **1**-**8**, among 32 sets of ΔE_{ST}^{CID}, many values such as $\Delta E_{1,2}^{CID}$ (−8.421 to −5.049 eV), $\Delta E_{1,4}^{CID}$ (-7.242 to −3.702 eV), and $\Delta E_{5,2}^{CID}$ (−6.002 to −0.132 eV), are negative, which are beneficial for the occurrence of IST energy gap. However, in molecules **9**-**12**, there are only a few negative values and their values are more than −3.045 eV, which makes it difficult to nurture IST energy gap. For example, molecule **6** has not only eleven highly negative ΔE_{ST}^{CID} modes with the lowest $\Delta E_{1,2}^{CID}$ of -6.206 eV, but also a very small ΔE_{ST}^{CIS} of 0.244 eV, which is a typical IST molecule (Fig. 2b). In contrast, molecule **11** has four negative ΔE_{ST}^{CID} modes ($\Delta E_{1,2}^{CID}$, $\Delta E_{1,3}^{CID}$, $\Delta E_{1,4}^{CID}$, $\Delta E_{2,2}^{CID}$) with the smallest $\Delta E_{1,2}^{CID}$ value of -1.128 eV, and a large ΔE_{ST}^{CIS} of 1.220 eV, making it a common PST molecule. To better illustrate all of this, we further analyze the $\Delta E_{1,2}^{CID}$, $\Delta E_{1,4}^{CID}$, and $\Delta E_{5,2}^{CID}$ with the lowest negative values, and display their components $\Delta\varepsilon$ ($\Delta\varepsilon_{1,2}$, $\Delta\varepsilon_{1,4}$, $\Delta\varepsilon_{5,2}$), ΔJ ($\Delta J_{1,2}$, $\Delta J_{1,4}$, $\Delta J_{5,2}$) and ΔK($\Delta K_{1,2}$, $\Delta K_{1,4}$, $\Delta K_{5,2}$) in Figs. 2d-2f and Table S11-S13. It is found that the ΔJ and ΔK are similar in molecules **1**-**12**, with their values mainly ranging from −2.000 to 2.000 eV. Differently, the $\Delta\varepsilon$ varies within a large range of −10.000–0.000 eV. It is very low in IST molecules (mostly below −4.000 eV), while it is much higher in PST molecules with values more than ca. -3.500 eV. Based on these results, it can be concluded that $\Delta\varepsilon$ is the most critical factor in generating the IST energy gap. Look into the definition of $\Delta\varepsilon$ given in the SI, they are $\Delta\varepsilon_{1,2} = \varepsilon_L - \varepsilon_{L+1} + 2(\varepsilon_{H-1} - \varepsilon_H)$, $\Delta\varepsilon_{1,4} = 2(\varepsilon_L - \varepsilon_{L+1}) + \varepsilon_{H-1} - \varepsilon_H$, $\Delta\varepsilon_{5,2} = 2(\varepsilon_{H-1} - \varepsilon_H)$. Trigged from these, we come up with$O_D = \varepsilon_L - \varepsilon_{L+1} + \varepsilon_{H-1} - \varepsilon_H$ as the other molecular descriptor for screening IST molecules.

So far, two molecular descriptors K_S and O_D, which are related to single electron and double electron excitations respectively, have been established for screening IST molecules. The competition between the exchange integral between orbitals in single excitation (positive value) and the energy gap between orbitals in double excitation (negative value) determines the occurrence of IST molecules. In addition, the python code for computing K_S and O_D is provided in SI, all parameters of K_S and O_D are calculated at HF level.

High-throughput virtual screening using these descriptors

From the above discussion, it can be known that small HOMO-LUMO exchange integral and double excitation are profit to induce the inversion of singlet and triplet states in energy. Heterocyclic triazene derivatives were reported to exhibit well-separated HOMO and LUMO and character of double excitations, which are the candidates for thermally activated delayed fluorescence materials[23,24]. Therefore, nine triazene cores are selected here to generate 3468 molecular cores by substituting different atoms in the ring (see Fig. 3a) using RDKit[25]. Then the high-throughput virtual screening is performed using K_S and O_D descriptors, and confirmed by post-HF methods, and the workflow is shown in Fig. 3b. Step I is the establishment of database. All the initial structures generated from 3486 SMILES strings are optimized and their frequencies are analyzed at B3LYP/cc-pVDZ level, and the unstable structures with imaginary frequencies are removed, 3156 stable structures are preserved. Step II is the molecular screening by molecular descriptors. The orbital energies of 3156 molecules are extracted and the descriptors K_S and O_D are calculated, and the 338 molecules are screened as potential IST candidates when they meet $K_S < 0.400$ eV and $O_D < -3.000$ eV. Step III is the verification of results. The S_1 and T_1 vertical excitation energy $\Delta E(S_0 \rightarrow S_1)$, $\Delta E(S_0 \rightarrow T_1)$ and vertical ΔE_{ST} are computed by using EOM-CCSD/cc-pVDZ and SC-NEVPT2(8,8)/cc-pVDZ methods to identify the final IST molecules. Finally, the emission properties of the winners are investigated.

Firstly, we analyze the K_S and O_D of 35 IST molecules reported in the literature and identify the conditions required to generate the IST energy gap (Figs. S26–S27). The results in Fig. S27 indicate that the values of K_S and O_D are almost always less than 0.400 eV and −3.000 eV, respectively, for all molecules. Therefore, $K_S < 0.400$ eV and $O_D < -3.000$ eV are used as the criteria for identifying IST molecules. According to these conditions, 338 molecules are screened from a total of 3156, as shown in Fig. 4a. Subsequently, the EOM-CCSD/cc-pVDZ method is adopted to calculate the vertical excitation energies of the S_1 and T_1 states and their differences ΔE_{ST} at the optimized S_0-geometry for these 338 molecules, as illustrated in Fig. 4b. From Fig. 4b, it is evident that 72 out of the 338 candidates exhibit negative ΔE_{ST} and are identified as IST molecules. Furthermore, the multireference SC-NEVPT2 (8,8)/cc-pVDZ method is used to refine the selection, resulting in 41 IST molecules from these 72 candidates (Fig. 4c). Due to limitations in computational resources, the choice of the SC-NEVPT2 (8,8) active space represents a balanced compromise between computational cost and accuracy. This descriptor-assisted screening method (DASM) takes a total of 2.8×10^3 h to screen 41 IST molecules from a combined pool of 3156 molecules.

To validate the accuracy and efficiency of the descriptors K_S and O_D, the EOM-CCSD/cc-pVDZ method is directly applied to calculate the ΔE_{ST}

Fig. 3 | 3486 virtual data set generation and a high-throughput virtual screening workflow establishment using our descriptors. **a** Chemical structures of 3486 candidates based on heterocyclic triazene derivatives. **b** Overview of the high-throughput virtual screening workflow using descriptor K_S and O_D.

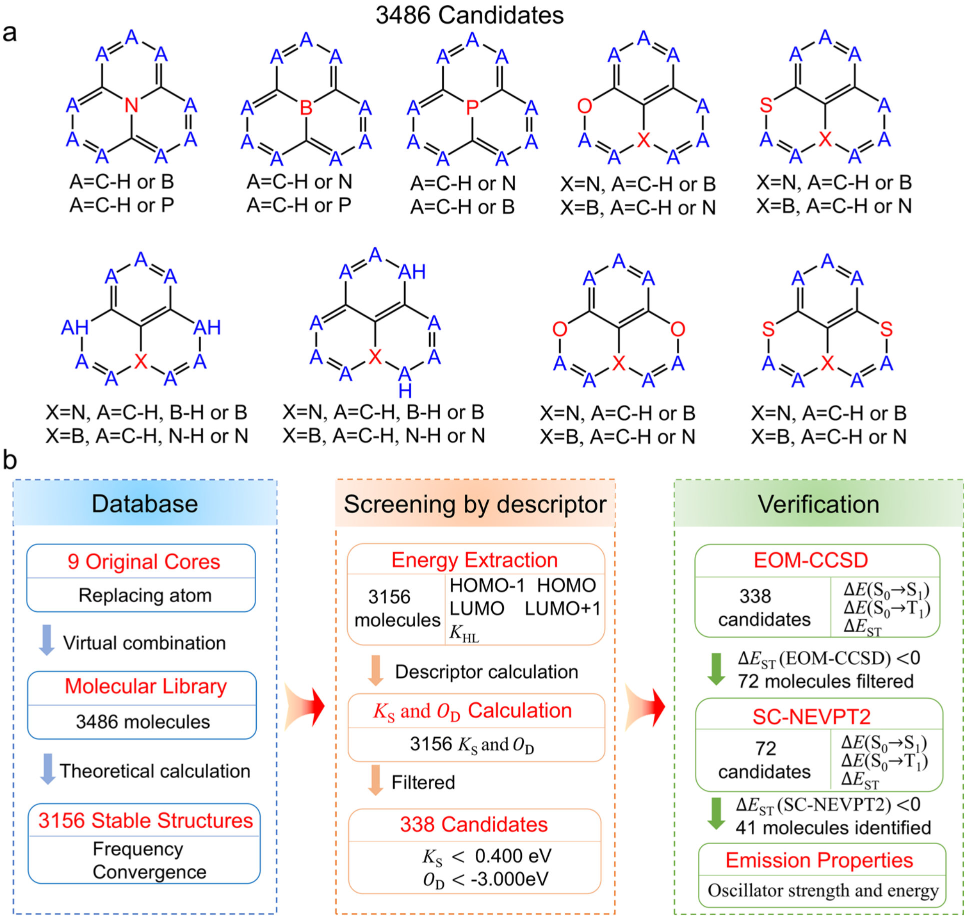
a
3486 Candidates
A=C-H or B
A=C-H or P
A=C-H or N
A=C-H or P
A=C-H or N
A=C-H or B
X=N, A=C-H or B
X=B, A=C-H or N
X=N, A=C-H or B
X=B, A=C-H or N
X=N, A=C-H, B-H or B
X=B, A=C-H, N-H or N
X=N, A=C-H, B-H or B
X=B, A=C-H, N-H or N
X=N, A=C-H or B
X=B, A=C-H or N
X=N, A=C-H or B
X=B, A=C-H or N
b
Database
9 Original Cores
Replacing atom
Virtual combination
Molecular Library
3486 molecules
Theoretical calculation
3156 Stable Structures
Frequency Convergence
Screening by descriptor
Energy Extraction
3156 molecules
HOMO-1 HOMO
LUMO LUMO+1
K_{HL}
Descriptor calculation
K_S and O_D Calculation
3156 K_S and O_D
Filtered
338 Candidates
K_S < 0.400 eV
O_D < -3.000eV
Verification
EOM-CCSD
338 candidates
$\Delta E(S_0 \rightarrow S_1)$
$\Delta E(S_0 \rightarrow T_1)$
ΔE_{ST}
ΔE_{ST}(EOM-CCSD) <0
72 molecules filtered
SC-NEVPT2
72 candidates
$\Delta E(S_0 \rightarrow S_1)$
$\Delta E(S_0 \rightarrow T_1)$
ΔE_{ST}
ΔE_{ST}(SC-NEVPT2) <0
41 molecules identified
Emission Properties
Oscillator strength and energy

Fig. 4 | Comparison of the descriptor-assisted screening method (DASM) and the full-calculation screening method (FCSM). **a** The K_S and O_D values of 3156 candidates. **b** The $\Delta E(S_0 \rightarrow S_1)$ and ΔE_{ST} values of 338 candidates at EOM-CCSD/cc-pVDZ level. **c** The $\Delta E(S_0 \rightarrow S_1)$ and ΔE_{ST} values of 72 candidates at SC-NEVPT2 (8,8)/cc-pVDZ level. **d** The $\Delta E(S_0 \rightarrow S_1)$ and ΔE_{ST} values of 3156 candidates at EOM-CCSD/cc-pVDZ level. **e** The $\Delta E(S_0 \rightarrow S_1)$ and ΔE_{ST} values of 117 IST candidates at SC-NEVPT2(8,8)/cc-pVDZ level. **f** The CPU times consumed by the DASM and the FCSM.

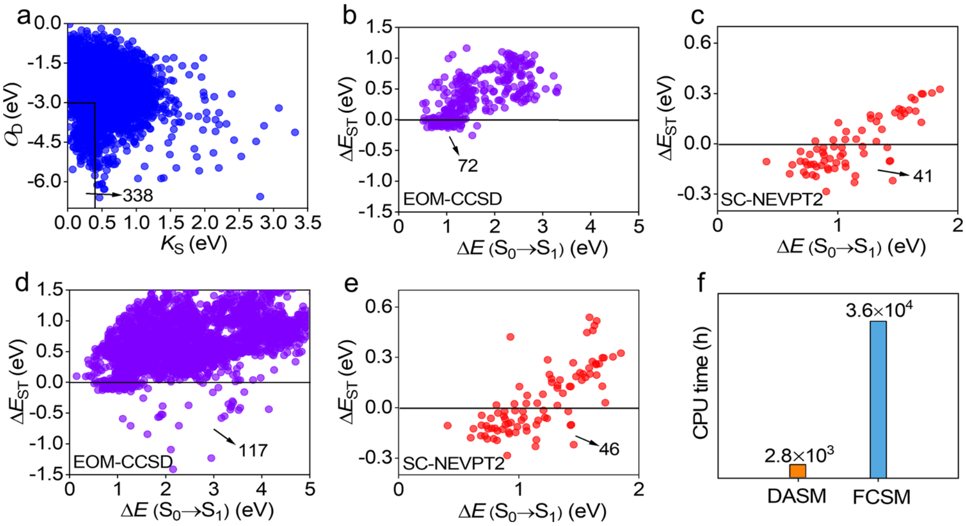

for all 3156 molecules. Among these, 117 molecules (**S36-S152** in Fig. S28) are identified with negative ΔE_{ST} (Fig. 4d). The values of the $\Delta E(S_0 \rightarrow S_1)$, $\Delta E(S_0 \rightarrow T_1)$ and ΔE_{ST} for these 117 molecules are listed in Table S14. As illustrated in Table S14, the $\Delta E(S_0 \rightarrow S_1)$ ranges from 0.521 to 4.161 eV, and the $\Delta E(S_0 \rightarrow T_1)$ varies between 0.551 and 4.609 eV, resulting in ΔE_{ST} ranging from -1.427 to -0.0002 eV. Similarly, the SC-NEVPT2(8,8) method is employed to further refine the selection, yielding 46 IST molecules from these 117 molecules (Fig. 4e and Table S15). To check the impact of the active space, the SC-NEVPT2(12,12) is also used for **M1-M46**, and the results (Table S16) are similar to those of SC-NEVPT2 (8,8). The molecular structures and ΔE_{ST} energies at the SC-NEVPT2(8,8)/cc-pVDZ level for these 46 IST molecules (**M1-M46**) are shown in Scheme 2. This full-calculation screening method (FCSM) takes a total of 3.6×10^4 h to screen 46 IST molecules from the pool of 3156 molecules, which is 13 times longer than the time required for the DASM described above. If the results of 46 IST molecules identified by FCSM are regarded as the standard, the success rate of DASM is close to 90%. These findings confirm that the DASM is both reliable and highly efficient.

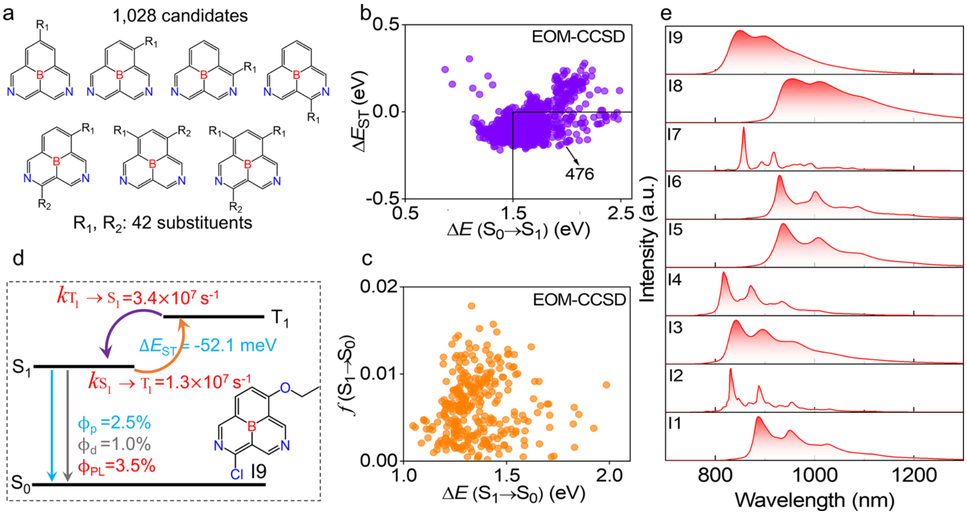

Fig. 5 | The virtual screening results from 1028 candidates. a Molecular structures of 1028 candidates based on **M3** cores. **b** The vertical ΔE_{ST} values and $\Delta E(S_0\to S_1)$ of 1028 candidates at EOM-CCSD/cc-pVDZ level. **c** The oscillator strength and $\Delta E(S_1\to S_0)$ of 476 IST molecules at EOM-CCSD/cc-pVDZ level. **d** Schematic diagram of the excited-state processes and the photophysical parameters of **I9**. **e** The photoluminescence spectra of molecules **I1**-**I9**.

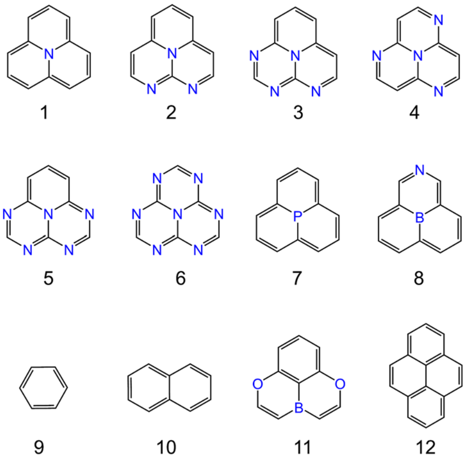
1
2
3
4
5
6
7
8
9
10
11
12

Scheme 1 | Chemical structures of the molecules 1-12 in four-orbital model (FOM). Molecules **1**-**8** with IST energy gap reported, and four common molecules **9**-**12** with normal PST energy gap.

For practical applications of IST molecules in OLEDs, their emissive properties are further investigated. The geometric structures of the S_1 and T_1 states are optimized at TD-B3LYP/cc-pVDZ level, and the emission energy ($\Delta E(S_1\to S_0)$), oscillator strength ($f(S_1\to S_0)$), and adiabatic ΔE_{ST} are calculated at EOM-CCSD/cc-pVDZ level for the 46 IST molecules. The results are given in Table S17 and Fig. S29. It is seen that the adiabatic ΔE_{ST} of all molecules are negative, expect for **M43**, the $\Delta E(S_1\to S_0)$ ranges from 0.160 to 1.316 eV, and the $f(S_1\to S_0)$ varies from 0.0000 to 0.0019. Among these, **M3** is a potential IST core with $\Delta E(S_1\to S_0)$ of 1.041 eV and $f(S_1\to S_0)$ up to 0.0019. Based on **M3**, 1,028 candidate molecules with fewer than 28 atoms are generated by introducing 42 substituents at different positions (Fig. 5a and S30). The S_0-geometries are optimized at B3LYP/cc-pVDZ level, and the corresponding vertical excitation energies $\Delta E(S_0\to S_1)$, $\Delta E(S_0\to T_1)$ and ΔE_{ST} are calculated at EOM-CCSD/cc-pVDZ level, as depicted in Fig. 5b. There appear 794 molecules with negative ΔE_{ST}. Herein, 476 molecules with $\Delta E(S_0\to S_1)\geq$ 1.5 eV are extracted for further calculations of emission energy and oscillator strength (Fig. 5c). As clearly shown in Fig. 5c, compared to **M3**, the $f(S_1\to S_0)$ values are promoted by an order of magnitude, up to 0.0178, which is a high value reported for near-infrared IST molecules in the references.

Furthermore, the luminescence properties of molecules **I1**-**I9** (Fig. S31) with the highest $f(S_1\to S_0)$ are investigated. The related energies, spin-orbit couplings, the rate constants of excited-state decays, and prompt and delayed photoluminescence quantum yields (PLQY) are summarized Tables S18-S21 and Fig. 5d. And the emissive spectra are plotted in Fig. 5e with the assignments of some typical peaks in Fig. S32. Their emissive spectra of these candidates are localized in the range from 862.4 to 1002.2 nm, and the spectral broad shapes mainly stem from the synergistic vibronic progressions of multiple modes. Their radiative rate constants k_r range from 1.0×10^6 s^{-1} to 9.7×10^6 s^{-1}, which is the largest ones for IST systems. Their nonradiative rate constant from S_1 to S_0 state k_{nr} varies from 1.0×10^7 s^{-1} to 6.0×10^8 s^{-1}, which is considerably small for near-infrared systems with so narrow energy gaps. As expected, their intersystem crossing rate constants from T_1 to S_1 ($k_{T_1\to S_1}$) always overwhelms the corresponding $k_{S_1\to T_1}$, which reflect the advantages of IST molecules. As a result, they exhibit high PLQYs. More surprisingly, among the similar IST molecules, there appear prompt and delayed fluorescence in **I4** and **I9** while there is only prompt fluorescence in the others. Among these compounds, **I9** has

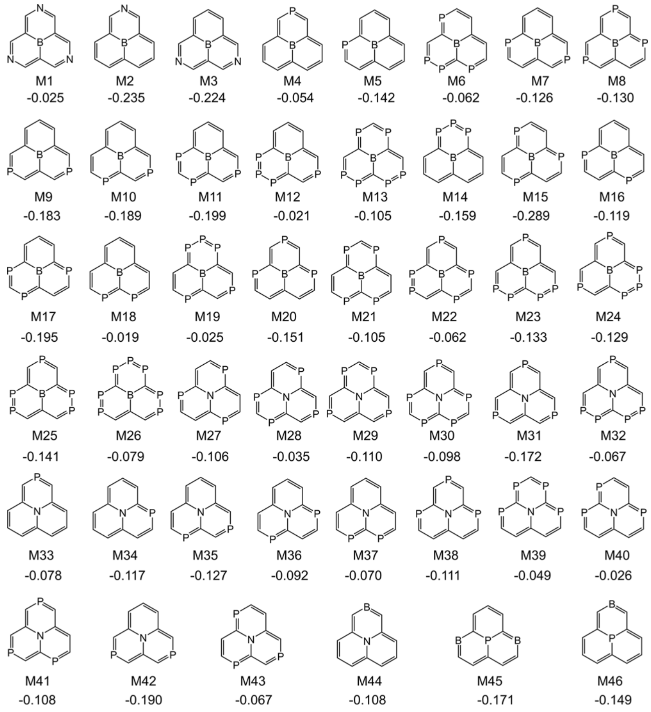
M1
-0.025
M2
-0.235
M3
-0.224
M4
-0.054
M5
-0.142
M6
-0.062
M7
-0.126
M8
-0.130
M9
-0.183
M10
-0.189
M11
-0.199
M12
-0.021
M13
-0.105
M14
-0.159
M15
-0.289
M16
-0.119
M17
-0.195
M18
-0.019
M19
-0.025
M20
-0.151
M21
-0.105
M22
-0.062
M23
-0.133
M24
-0.129
M25
-0.141
M26
-0.079
M27
-0.106
M28
-0.035
M29
-0.110
M30
-0.098
M31
-0.172
M32
-0.067
M33
-0.078
M34
-0.117
M35
-0.127
M36
-0.092
M37
-0.070
M38
-0.111
M39
-0.049
M40
-0.026
M41
-0.108
M42
-0.190
M43
-0.067
M44
-0.108
M45
-0.171
M46
-0.149

Scheme 2 | The identified IST molecular cores. The molecular structures of 46 IST molecular cores and their vertical ΔE_{ST} (eV) at SC-NEVPT2(8,8)/cc-pVDZ level.

the highest PLQY of 3.5%, in which the prompt and delayed PLQY are 2.5% and 1.0%, respectively, as shown in Fig. 5d. Overall, a series of potential non-traditional near-infrared IST emitters are predicted, and their quantum efficiencies are satisfactory compared with traditional near-infrared systems.

Summary

In this work, we have devised a four-orbital model (FOM) to elucidate in detail the roles of single and double excitations in the IST formation in azaphenalene derivatives. Importantly, under this model we have constructed two descriptors (K_S and O_D) based on molecular frontier orbital energy and exchange integral, which can be easily obtained by simple quantum chemistry calculation for molecules in the ground state. Out of a dataset of 3,486 molecules, 41 IST molecular cores are identified using the descriptor-assisted screening method, and verified with the state-of-the-art methods. Compared with the results of the full-calculation screening method, the accuracy of descriptor-assisted method is 90% with a speed nearly 13 times faster. Furthermore, starting from the IST molecular core with the largest oscillator strength, 1028 candidate molecules are generated by introducing 42 substituents, and their photophysical properties are investigated by combining post-HF method and thermal vibration correlation function rate theory. And a series of potential near-infrared IST emitters are predicted with emission wavelength ranging from 852.2 to 1002.3 nm and the highest PLQY of 3.5% at 880.7 nm, which can match and outperform the currently reported traditional near-infrared fluorescence systems in quantum efficiencies. This work provides a deeper understanding of the origin of energy inversion in IST molecules, and offers valuable insights for future molecular design. This work not only marks the first time that IST materials have been predicted and proposed as near-infrared OLED emitters but also paves the way for practical applications in areas such as biomedicine and component determination. However, these descriptors would limit to triangulene-based systems, and not suitable for other types of IST systems. In the future, we will develop general descriptors and machine learning models for high-throughput screening IST candidates in more diverse datasets.

Methods

The wave functions and excitation energy expression

The wave functions $|{}^1\Psi_H^L\rangle$ and $|{}^3\Psi_H^L\rangle$ of the S_1 and T_1 states by CIS theory can be expressed as:

$$|{}^1\Psi_H^L\rangle = \frac{1}{\sqrt{2}}(|\bar{H}L + |H\bar{L}), \tag{4}$$

$$|{}^3\Psi_H^L\rangle = \frac{1}{\sqrt{2}}(|\bar{H}L - |H\bar{L}). \tag{5}$$

Here, the $\bar{H}$, $\bar{L}$ and H, L indicate orbitals with α and β spin components, respectively. The corresponding energies of singlet and triplet states can be calculated as:

$$E_{\mathrm{S}}^{\mathrm{CIS}} = \langle {}^1\Psi_H^L|\hat{H} - E_0|{}^1\Psi_H^L\rangle = \varepsilon_{\mathrm{L}} - \varepsilon_{\mathrm{H}} + 2K_{\mathrm{H,L}} + J_{\mathrm{H,L,}} \tag{6}$$

$$E_T^{\mathrm{CIS}} = \langle {}^3\Psi_H^L|\hat{H} - E_0|{}^3\Psi_H^L\rangle = \varepsilon_L - \varepsilon_H + J_{H,L}. \tag{7}$$

And their energy difference is:

$$\Delta E_{\mathrm{ST}}^{\mathrm{CIS}} = E_{\mathrm{S}}^{\mathrm{CIS}} - E_{\mathrm{T}}^{\mathrm{CIS}} = 2K_{\mathrm{HL}}. \tag{8}$$

The wave functions $|{}^1\Psi_{H,H}^{L,L}\rangle$ and $|{}^3\Psi_{H,H}^{L,L+1}\rangle$ of the S_1 and T_1 states by CID theory can be expressed as:

$$|{}^1\Psi_{H,H}^{L,L}\rangle = |\bar{L}L\rangle, \tag{9}$$

$$|{}^3\Psi_{H,H}^{L,L+1}\rangle = (|\bar{L}L + 1\rangle + |L\bar{+}1L\rangle). \tag{10}$$

For the detailed expression of $\Delta E_{1,1}^{\mathrm{CID}} = \Delta\varepsilon_{1,1} + \Delta J_{1,1} + \Delta K_{1,1}$ as:

$$\Delta\varepsilon_{1,1} = \varepsilon_{\mathrm{L}} - \varepsilon_{\mathrm{L+1}} + 2(\varepsilon_{\mathrm{H-1}} - \varepsilon_{\mathrm{H}}), \tag{11}$$

$$\Delta J_{1,1} = J_{\mathrm{H,H}} - J_{\mathrm{H-1,H-1}} + 2J_{\mathrm{H-1,L+1}} - J_{\mathrm{L,L+1}} + 2J_{\mathrm{H-1,L}} + J_{\mathrm{L,L}} - 4J_{\mathrm{H,L,}} \tag{12}$$

$$\Delta K_{1,1} = K_{\mathrm{H,L}} + K_{\mathrm{L,L+1}} - K_{\mathrm{H-1,L+1}} - K_{\mathrm{H-1,L.}} \tag{13}$$

Electronic structure calculation

The geometries of all molecules in their S_0, S_1 and T_1 states are optimized at the (TD) B3LYP/cc-pVDZ level using the Gaussian 16 program package[26]. The vertical excitation energies and the configurations of single and double excitations for molecules **1**-**12** in both S_1 and T_1 states are determined using the ADC(2)/cc-pVDZ method within the Q-Chem 5.2 software[27], the energy calculation at the EOM-CCSD/cc-pVDZ level is also performed on Q-Chem 5.2. The SC-NEVPT2/cc-pVDZ method utilizing CASSCF calculations based on MP2 natural orbitals in ORCA 6.0.1 software package[28], the SOC matrix elements based on T_1-geometries are computed at SC-NEVPT2/cc-pVDZ level using ORCA 6.0.1 package. Additionally, the Coulomb and exchange integrals for all molecules are analyzed at the HF/cc-pVDZ level, based on B3LYP-optimized geometries, employing the Multiwfn program[29]. We carry out the reorganization energy analysis between the S_0 and S_1 states at S_1-geometries using the molecular material property prediction package MOMAP 2022B[30–32]. The computational system of the server is based on the CPU model: Intel® Xeon® Platinum 8160 processor.

Photophysical properties calculation

The photoluminescence quantum yields of the prompt and delayed components (Φ_{p} and Φ_{d}) are given by[33]:

$$\Phi\mathrm{p} = \frac{k_{\mathrm{r}}}{k_{\mathrm{r}} + k_{\mathrm{nr}} + k_{\mathrm{S_1 \to T_1}}} \tag{14}$$

$$\boldsymbol{\Phi}\mathrm{d} = \sum_{k=1}^{\infty} (\boldsymbol{\Phi}_{\mathrm{S_1 \to T_1}} \times \boldsymbol{\Phi}_{\mathrm{T_1 \to S_1}})^k \boldsymbol{\Phi}\mathrm{p} \tag{15}$$

Here $\boldsymbol{\Phi}_{\mathrm{S_1 \to T_1}}$ and$\boldsymbol{\Phi}_{\mathrm{T_1 \to S_1}}$ are the quantum efficiencies for ISC and reverse ISC, respectively. The radiative decay k_{r} from S_1 to S_0 state is computed using $k_{\mathrm{r}} = f\Delta E^2/1.499$[34], in which f and ΔE are the oscillator strength and emission energy in cm^{-1}, respectively. The non-radiative decay k_{nr} from S_1 to S_0 state, $k_{\mathrm{S_1 \to T_1}}$ from S_1 to T_1 state and $k_{\mathrm{T_1 \to S_1}}$ from T_1 to S_1 state, and the emissive spectra are evaluated via the thermal vibration correlation function (TVCF) method in MOMAP 2022B.

Data availability

The authors declare that the necessary data supporting the findings of this study are available within the paper (and its Supplementary Information files). All data are available from the corresponding author upon reasonable request. The Python code for calculating molecular descriptor is available at Supplementary information.

Code availability

The Python code for calculating molecular descriptor is available at Supplementary information.

Received: 27 March 2025; Accepted: 3 September 2025;
Published online: 20 October 2025

References

1. Hong, G. et al. Brief history of OLEDs-Emitter development and industry milestones. *Adv. Mater.* **33**, 2005630 (2021).
2. Gu, G. et al. High-external-quantum-efficiency organic light-emitting devices. *Opt. Lett.* **22**, 396–398 (1997).
3. Shuai, Z. & Peng, Q. Organic light-emitting diodes: theoretical understanding of highly efficient materials and development of computational methodology. *Natl. Sci. Rev.* **4**, 224–239 (2017).
4. Uoyama, H. et al. Highly efficient organic light-emitting diodes from delayed fluorescence. *Nature* **492**, 234–238 (2012).
5. Li, P., Feng, L., Li, G. & Bai, Q. Effects of electron donating ability of substituents and molecular conjugation on the electronic structures of organic radicals. *Chem. Res. Chin. Univ.* **39**, 202–207 (2023).
6. Murawski, C., Leo, K. & Gather, M. C. Efficiency roll-off in organic light-emitting diodes. *Adv. Mater.* **25**, 6801–6827 (2013).
7. de Silva, P. Inverted singlet-triplet gaps and their relevance to thermally activated delayed fluorescence. *J. Phys. Chem. Lett.* **10**, 5674–5679 (2019).
8. Ehrmaier, J. et al. Singlet-triplet inversion in heptazine and in polymeric carbon nitrides. *J. Phys. Chem. A* **123**, 8099–8108 (2019).
9. Pollice, R., Friederich, P., Lavigne, C., Gomes, G. D. P. & Aspuru-Guzik, A. Organic molecules with inverted gaps between first excited singlet and triplet states and appreciable fluorescence rates. *Matter* **4**, 1654–1682 (2021).
10. Omar, O. H., Xie, X., Troisi, A. & Padula, D. Identification of unknown inverted singlet-triplet cores by high-throughput virtual screening. *J. Am. Chem. Soc.* **145**, 19790–19799 (2023).
11. Pollice, R., Ding, B. & Aspuru-Guzik, A. Rational design of organic molecules with inverted gaps between the first excited singlet and triplet. *Matter* **7**, 1161–1186 (2024).
12. Aizawa, N. et al. Delayed fluorescence from inverted singlet and triplet excited states. *Nature* **609**, 502–506 (2022).
13. Sancho-García, J. C. et al. Violation of Hund's rule in molecules: predicting the excited-state energy inversion by TD-DFT with double-hybrid methods. *J. Chem. Phys.* **156**, 034105 (2022).
14. Drwal, D. et al. Role of spin polarization and dynamic correlation in singlet-triplet gap inversion of heptazine derivatives. *J. Chem. Theory Comput.* **19**, 7606–7616 (2023).
15. Ghosh, S. & Bhattacharyya, K. Origin of the failure of density functional theories in predicting inverted singlet-triplet gaps. *J. Phys. Chem. A* **126**, 1378–1385 (2022).
16. Blaskovits, J. T., Corminboeuf, C. & Garner, M. H. Excited-state Hund's rule violations in bridged [10]- and [14] annulene perimeters. *J. Phys. Chem. A* **128**, 10404–10412 (2024).
17. Bedogni, M., Giavazzi, D., Maiolo, F. D. & Painelli, A. Shining light on inverted singlet-triplet emitters. *J. Chem. Theory Comput.* **20**, 902–913 (2024).
18. Sobolewski, A. L. & Domcke, W. Are heptazine-based organic light-emitting diode chromophores thermally activated delayed fluorescence or inverted singlet-triplet systems?. *J. Phys. Chem. Lett.* **12**, 6852–6860 (2021).
19. Ricci, G., Sancho-García, J.-C. & Olivier, Y. Establishing design strategies for emissive materials with an inverted singlet-triplet energy gap (INVEST): a computational perspective on how symmetry rules the interplay between triplet harvesting and light emission. *J. Mater. Chem. C.* **10**, 12680–12698 (2022).
20. Blaskovits, J. T., Garner, M. H. & Corminboeuf, C. Symmetry-induced singlet-triplet inversions in non-alternant hydrocarbons. *Angew. Chem. Int. Ed.* **135**, e202218156 (2023).
21. Jorner, K., Pollice, R., Lavigne, C. & Aspuru-Guzik, A. Ultrafast computational screening of molecules with inverted singlet-triplet energy gaps using the Pariser-Parr-Pople semiempirical quantum chemistry method. *J. Phys. Chem. A* **128**, 2445–2456 (2024).
22. Loos, P. F., Lipparini, F. & Jacquemin, D. Heptazine, cyclazine, and related compounds: chemically-accurate estimates of the inverted singlet-triplet gap. *J. Phys. Chem. Lett.* **14**, 11069–11075 (2023).
23. Hatakeyama, T. et al. Ultrapure blue thermally activated delayed fluorescence molecules: efficient HOMO-LUMO separation by the multiple resonance effect. *Adv. Mater.* **28**, 2777–2781 (2016).
24. Suresh, S. M., Hall, D., Beljonne, D., Olivier, Y. & Zysman-Colman, E. Multiresonant thermally activated delayed fluorescence emitters based on heteroatom-doped nanographenes: recent advances and prospects for organic light-emitting diodes. *Adv. Funct. Mater.* **30**, 1908677 (2020).
25. RDKit. https://github.com/rdkit/rdkit.
26. Frisch, M. J. et al. *Gaussian 16 Rev. C.01* (Gaussian, Inc., 2016).
27. Shao, Y. et al. Advances in molecular quantum chemistry contained in the Q-Chem 4 program package. *Mol. Phys.* **113**, 184–215 (2015).
28. Neese, F. Software update: the ORCA program system-version 5.0. *WIREs Comput. Mol. Sci.* **12**, e1606 (2022).
29. Lu, T. & Chen, F. Multiwfn: a multifunctional wavefunction analyzer. *J. Comput. Chem.* **33**, 580–592 (2012).
30. Peng, Q., Yi, Y., Shuai, Z. & Shao, J. Toward quantitative prediction of molecular fluorescence quantum efficiency: role of Duschinsky rotation. *J. Am. Chem. Soc.* **129**, 9333–9339 (2007).
31. Peng, Q. et al. Theoretical predictions of red and near-infrared strongly emitting X-annulated rylenes. *J. Chem. Phys.* **134**, 074510 (2011).
32. Shuai, Z. Thermal vibration correlation function formalism for molecular excited state decay rates. *Chin. J. Chem.* **38**, 1223–1232 (2020).
33. Goushi, K., Yoshida, K., Sato, K. & Adachi, C. Organic light-emitting diodes employing efficient reverse intersystem crossing for triplet-to-singlet state conversion. *Nat. Photonics* **6**, 253–258 (2012).
34. Hilborn, R. C. Einstein coefficients, cross sections, *f* values, dipole moments, and all that. *Am. J. Phys.* **50**, 982–986 (1982).

Acknowledgements

The authors are deeply indebted to Prof. Sergey Bokarev, Prof. Wolfgang Domcke, and Xuexiao Yang for valuable discussions and acknowledge the financial support from the National Natural Science Foundation of China (Grant Nos. 22325305 and 22273105), the Strategic Priority Research Program of Sciences (XDB0520103), National Key R&D Program of China (2024YFB3614300) and the Fundamental Research Funds for the Central Universities (Grant Nos. E2E40307X2 and E2ET0309X2). We gratefully acknowledge WQ & UCAS Research Academy Intelligent Computing Center (WRA-ICC) for providing computation facilities.

Author contributions

Q.P. designed the research program and analyzed the computational data. Y.P. implemented the computational program, derived the initial theoretical results, and wrote the original manuscript. J.W. and J.Y. provided some software support. Q.P. and Y.P. reviewed the paper.

Competing interests

The authors declare no competing interests.

Additional information

Supplementary information The online version contains supplementary material available at https://doi.org/10.1038/s41524-025-01792-2.

Correspondence and requests for materials should be addressed to Qian Peng.

Reprints and permissions information is available at
http://www.nature.com/reprints

Publisher's note Springer Nature remains neutral with regard to jurisdictional claims in published maps and institutional affiliations.

Open Access This article is licensed under a Creative Commons Attribution-NonCommercial-NoDerivatives 4.0 International License, which permits any non-commercial use, sharing, distribution and reproduction in any medium or format, as long as you give appropriate credit to the original author(s) and the source, provide a link to the Creative Commons licence, and indicate if you modified the licensed material. You do not have permission under this licence to share adapted material derived from this article or parts of it. The images or other third party material in this article are included in the article's Creative Commons licence, unless indicated otherwise in a credit line to the material. If material is not included in the article's Creative Commons licence and your intended use is not permitted by statutory regulation or exceeds the permitted use, you will need to obtain permission directly from the copyright holder. To view a copy of this licence, visit http://creativecommons.org/licenses/by-nc-nd/4.0/.

© The Author(s) 2025